Stability of Lobed Balloons

M. Pagitz Y. Xu S. Pellegrino *

Department of Engineering, University of Cambridge, Trumpington Street, Cambridge, CB2 1PZ, UK

Abstract

This paper presents a computational study of the stability of simple lobed balloon structures. Two approaches are presented, one based on a wrinkled material model and one based on a variable Poisson's ratio model that eliminates compressive stresses iteratively. The first approach is used to investigate the stability of both a single isotensoid and a stack of four isotensoids, for perturbations of infinitesimally small amplitude. It is found that both structures are stable for global deformation modes, but unstable for local modes at sufficiently large pressure. Both structures are stable if an isotropic model is assumed. The second approach is used to investigate the stability of the isotensoid stack for large shape perturbations, taking into account contact between different surfaces. For this structure a distorted, stable configuration is found. It is also found that the volume enclosed by this configuration is smaller than that enclosed by the undistorted structure.

Key words: balloon, isotensoid, membrane, stability, wrinkle.

1 Introduction and Background

Lobed, or "pumpkin", design shapes are widely used in long-duration ballooning. The main characteristic of a lobed balloon is the presence of high-curvature lobes formed by thin plastic foils bulging between stiff load-carrying tapes, instead of the convex, smooth shape of, e.g. hot-air balloons. The pumpkin shape, although attractive in terms of pressure-carrying efficiency and statically-determinate stress distribution, has been found to be unstable in some cases, with the result that several balloons have taken up a distorted, non-symmetrical configuration, upon inflation (Nott 2004).

* Corresponding author.
Email address: sp28@cam.ac.uk (S. Pellegrino).

Calladine (1988) explained this behaviour by showing that the volume enclosed by a lobed balloon increases —if the number of lobes and the bulge formed by the lobes are sufficiently large— for certain small-amplitude inextensional deformations of the balloon. This led to a stability criterion for pumpkin balloons based on an analogy between the geometric stiffness of a lobe of a balloon and the elastic bending stiffness of an Euler strut. An experimental study of balloons designed to lie on either side of Calladine's stability boundary was carried out by Schur (2004).

A detailed, semi-analytical study of the variation of the volume enclosed by inextensional pumpkin balloons, with different number of lobes and different, finite amounts of bulging in each lobe, was carried out by Lennon and Pellegrino (2000). This study examined the variation in the volume enclosed by several pumpkin balloons, for certain prescribed deformation modes. Although the volume was found to always decrease for small distortions, it increased when a sufficiently large distortion was imposed. However, equilibrium considerations were neglected in this study, despite the finite magnitude of the shape changes considered.

A more realistic model of a pumpkin balloon, which can hence provide actual estimates of the stability of a particular design shape, requires a more detailed approach, which can only be pursued using sophisticated, and complex, computer tools. There are two key effects that need to be taken into account, the tension-only behaviour of thin foils, and contact between different parts of the surface of a balloon.

Two geometrically non-linear finite-element models of a balloon structure will be presented, which address these issues. The results obtained from these models will be compared with existing analytical solutions for the shape and stress distribution of pumpkin balloons, and provide considerable insight into their stability.

The first model is based on a novel finite-element formulation for heavily wrinkled membranes. It allows us to set up pressurized balloons where the stress path is specified. Once the initial shape and stress distribution of a balloon are known, the tangent stiffness matrix for the balloon is set up and the stability of the balloon for small perturbations is analysed by computing the eigenvalues of the stiffness matrix.

The second model is based on the variable Poisson's ratio approach proposed by Stein and Hedgepeth (1961), and its finite element implementation by Miller and Hedgepeth (1982) and Miller et al. (1985). An implementation of this approach through the Iterative Modified Properties (IMP) user-defined subroutine in ABAQUS by Adler (2000) has been modified to deal with membrane structures that are prestressed uniaxially, i.e. the minor principal stress

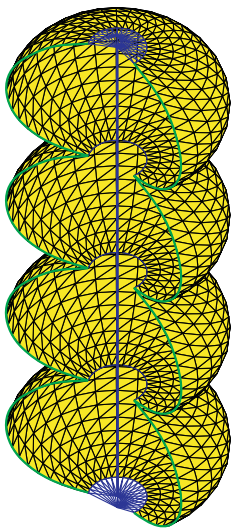

Fig. 1. Lobed cylinder.

is zero. ABAQUS does not compute the eigenvalues of a non-symmetric stiffness matrix (as it is the case for a pressure-loaded structure) but the ABAQUS surface-contact model is very useful to study the stability of a balloon for finite perturbations.

This paper is presented in seven sections. The particular type of lobed balloon that is to be investigated is presented in the next section. It is a simpler structure than the pumpkin balloons that are of current, practical interest, but its behaviour has many of the features observed in practice. Then, Sections 3 and 4 present the two computational models that have been developed. Section 5 studies the initial stability of the balloon structure by means of the first computer model, for varying internal pressure and considering two different material models. Section 6 studies the stability of the balloon for large distortions, by means of the second computer model. Section 7 concludes the paper.

2 Lobed Cylinder

The structure whose stability will be studied in this paper is a weightless "lobed cylinder" subject to uniform internal pressure. This cylinder is formed by stacking a number of (mostly four) identical truncated isotensoids, reinforcing the seam lines, closing them off at the top and bottom with rigid plates, and holding the ends of the two plates at a fixed distance by means of a pin-jointed bar, see Figure 1.

Structures resembling this one, but with meridians of circular profile, were studied by Calladine (1988) and Lennon and Pellegrino (2000). These studies

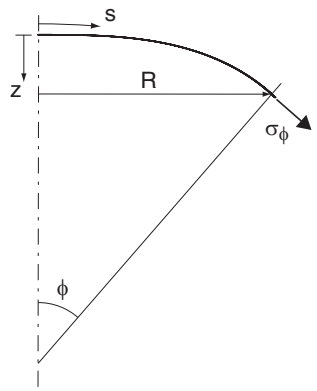

Fig. 2. Definition of coordinate system and meridional stress.

showed that the sign of the rate of change of the enclosed volume (for an assumed mode involving the axis of the stack bending into a circular arc) depends on the number of elements in the stack and the amount of bulging of the cylinder. Hence, the initial configuration can be either stable or unstable depending on the value of these parameters.

The lobed cylinder that is studied in this paper is formed starting from the isotensoid, which is the shape of the axisymmetric surface that carries a uniform pressure purely by meridional stress (Taylor 1919), i.e. the hoop stress is zero everywhere. The meridian of the isotensoid is defined by the radius, R, and vertical distance from the apex, z, as shown in Figure 2

$$R = R_0 \,\mathrm{cn}(u) \tag{1}$$

and

$$z = -\frac{R_0}{\sqrt{2}}\Big\{2\big[E - \mathrm{E}(u)\big] - (K - u)\Big\} \tag{2}$$

where

$$u = K - \frac{s\sqrt{2}}{R_0} \tag{3}$$

Here cn is one of the Jacobi elliptic functions and $\mathrm{E}(u)$ is the complete elliptic integral of the second kind, for modulus u; $K = 1.8541$ and $E = 1.3506$; R_0 is the radius at the equator; and s is the arc-length along the meridian, measured from the axis.

These equations can be evaluated using the functions `ellipj` and `ellipke` in Matlab (Mathworks 2002).

The meridian of an isotensoid with a radius at the equator of one unit is shown in Figure 3. The extreme values of z/R_0 are ± 0.598.

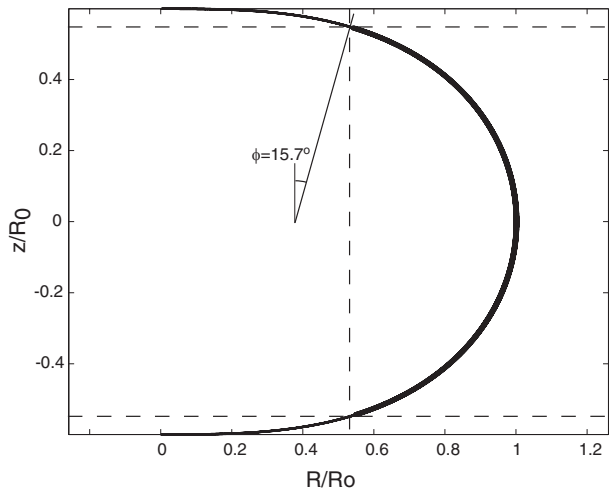

Fig. 3. Meridian of an isotensoid.

For a given uniform pressure, p, the meridional stress σ_ϕ is given by

$$\sigma_\phi = \frac{pR}{2t \sin \phi} \tag{4}$$

The building block for our lobed cylinder is obtained by truncating an isotensoid, i.e. by slicing off the top and bottom caps and leaving only the region $-z_0 \leq z \leq z_0$, where $z_0/R_0 = 0.55$, see Figure 3. The value of the angle ϕ at the truncation point is $\phi = 15.7$ deg. Note that from now on the origin of the z-axis will be moved to the top of the stack of truncated isotensoids, but the same symbol will be used to denote this new coordinate.

Clearly, a truncated isotensoid is not in equilibrium unless a suitable distribution of meridional forces is applied along the edge of the cuts. These forces are applied either by the neighbouring isotensoids, or by additional structural elements, as shown in Figure 4. First, consider the seam line between two neighbouring truncated isotensoids. Denoting by N_r and N_v respectively the radial and vertical components of the force per unit length along the cuts, note that the N_v's are in equilibrium and the N_r's add to provide an in-plane radial load of $2N_r$ on the seam line. By arranging an extensionally stiff circular hoop along the seam, this load can be carried without significant deformation.

Next, consider the truncated isotensoid at the top of the stack. Here there is only one N_v and so, to ensure equilibrium, a stiff circular plate is arranged to carry both the in-plane radial loads N_r and the out-of-plane shear loads N_v. Vertical equilibrium of this plate is ensured by a compressive axial force in the rod, along the axis of the stack.

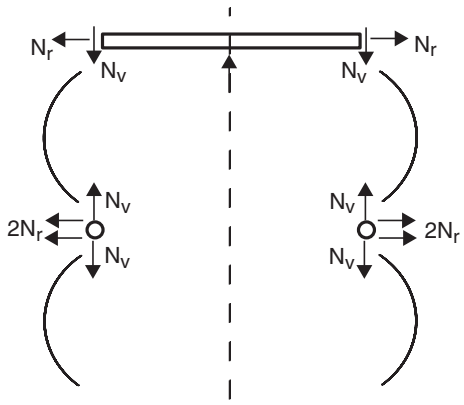

Fig. 4. Free body diagrams for seam line and end plate.

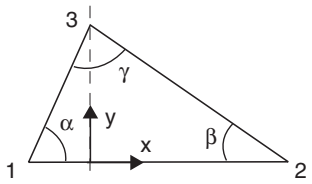

Fig. 5. Wrinkled element local coordinate system.

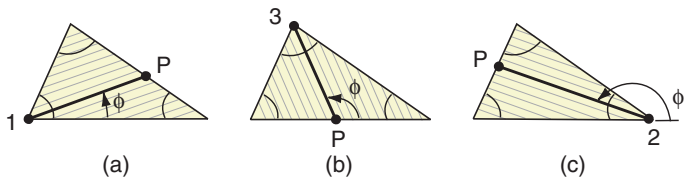

Fig. 6. Wrinkle directions.

3 Wrinkled Membrane Model

We have formulated a novel three-node, constant-stress, constant strain, wrinkled membrane element. This element is formulated in the local coordinate system shown in Figure 5, and the wrinkle direction is defined by the angle ϕ between side 1-2 and the direction of the wrinkle. Depending on whether (a) $0 \leq \phi \leq \alpha$, (b) $\alpha \leq \phi \leq \alpha + \gamma$, or (c) $\alpha + \gamma \leq \phi \leq \pi$, we choose a reference wrinkle that emanates from node 1, 3, or 2, as shown in Figure 6.

This element has a rank-deficient stiffness matrix, due to the presence of two internal zero-energy modes, as shown in Figure 7. Mode (a) stretches the element in the direction perpendicular to the wrinkles, mode (b) shears the wrinkles. Only mode (c), which stretches the element in the direction of the wrinkles, induces a change of strain energy.

The displacement field within the element is linear, and hence the strain is uniform. The directions of principal strain are assumed to coincide with the direction of the wrinkles and the direction perpendicular to them. The Green-

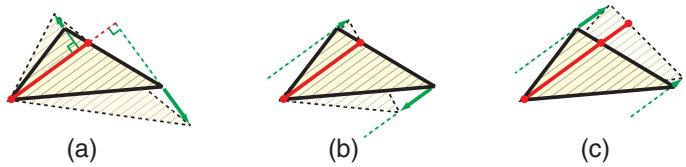

Fig. 7. Deformation modes of wrinkled element.

Lagrange strain, ϵ_w, along the reference wrinkle is found, depending on the wrinkle angle ϕ defined in Figure 6, by considering the line iP, where i is node 1, 2, or 3.

The corresponding linear-elastic stress along the wrinkle is found from

$$\sigma_w = E\epsilon_w \tag{5}$$

where E is the Young's Modulus of the material.

The strain components in the element coordinate system are found from a standard strain transformation, where the strain perpendicular to the wrinkle is taken as zero, and the corresponding stress components are found similarly, by taking the stress perpendicular to the wrinkle also to be zero. Hence, letting $c = \cos\phi$ and $s = \sin\phi$

$$\begin{bmatrix} \epsilon_x \\ \epsilon_y \\ \gamma_{xy} \end{bmatrix} = \begin{bmatrix} c^2 \\ s^2 \\ 2cs \end{bmatrix} \epsilon_w \tag{6}$$

where γ_{xy} is the engineering shear strain, and

$$\begin{bmatrix} \sigma_x \\ \sigma_y \\ \sigma_{xy} \end{bmatrix} = \begin{bmatrix} c^2 \\ s^2 \\ cs \end{bmatrix} \sigma_w \tag{7}$$

Therefore, considering an initially prestressed membrane,

$$\begin{bmatrix} \sigma_x \\ \sigma_y \\ \sigma_{xy} \end{bmatrix} = D \begin{bmatrix} \epsilon_x \\ \epsilon_y \\ \gamma_{xy} \end{bmatrix} + \begin{bmatrix} \sigma_{x0} \\ \sigma_{y0} \\ \sigma_{xy0} \end{bmatrix} \tag{8}$$

where

$$D = E \begin{bmatrix} c^4 & c^2s^2 & c^3s \\ c^2s^2 & s^4 & cs^3 \\ c^3s & cs^3 & c^2s^2 \end{bmatrix} \tag{9}$$

and $[\sigma_{x0}\ \sigma_{y0}\ \sigma_{xy0}]^T$ are the components of prestress along the wrinkles, transformed to the element coordinate system.

Further details on this element, including the material and geometric stiffness matrices from which an iterative Newton-Raphson equilibrium iteration can be set up, will be published elsewhere. The formulation of this element also includes the computation of its non-symmetric load-stiffness matrix, which accounts for the follower-type load applied by the internal pressure.

4 Non-Linear Material Model

Miller and Hedgepeth (1982) and Miller et al. (1985) proposed a finite element implementation of the Stein-Hedgepeth (1961) wrinkle model. This model is based on the observation that in a wrinkled element the geometric strain in the direction perpendicular to the direction of the wrinkles —due to the material deforming out-of-plane— can be modelled by introducing a variable effective Poisson's ratio for the membrane.

Hence, instead of the standard modulus matrix based on Hooke's law for plane stress

$$D_t = \frac{E}{1-\nu^2}\begin{bmatrix} 1 & \nu & 0 \\ \nu & 1 & 0 \\ 0 & 0 & (1-\nu)/2 \end{bmatrix} \tag{10}$$

which is used in the regions where the membrane is taut, they used the matrix

$$D_w = \frac{E}{4}\begin{bmatrix} 2(1+P) & 0 & Q \\ 0 & 2(1-P) & Q \\ Q & Q & 1 \end{bmatrix} \tag{11}$$

where $P = (\epsilon_x - \epsilon_y)/(\epsilon_1 - \epsilon_2)$ and $Q = \gamma_{xy}/(\epsilon_1 - \epsilon_2)$. 1 and 2 are the directions parallel and perpendicular to the wrinkles, respectively, and are allowed to rotate as the stress state changes.

Adler (2000) implemented this model as a user-defined material (UMAT) subroutine in the ABAQUS (2003) finite element package. At any stage of a standard ABAQUS iteration, given the current strain and strain increment in an an element, this subroutine works out the corresponding stress components using either D_t or D_w, depending on the state of the element.

Specifically, Adler's IMP subroutine begins by calculating the principal strain and stresses using D_t, i.e. assuming the element to be taut, and then (denoting by 1, 2 the major and minor principal stress/strain directions, respectively)

- If $\sigma_2 \geq 0$, then the element is taut and so no change is needed;
- If $\sigma_2 < 0$ and $\epsilon_1 \leq 0$, then the element is slack and so all stress components are zero;
- If $\sigma_2 < 0$ and $\epsilon_1 > 0$, then the element is wrinkled, and so the stress components are recomputed using D_w.

We have modified this subroutine so that we can prescribe a load-carrying path in a structure. Hence, to set up the correct pressure-induced stresses in an isotensoid, we initially define all elements with their local y-axis in the hoop direction. Then, when $\sigma_2 \geq 0$ (i.e. case 1 in Adler's subroutine), we set $\sigma_y = 0$ and leave σ_x and σ_{xy} unchanged.

Thus, once the correct initial stresses have been set up, we switch to the standard IMP subroutine used by Adler.

4.1 Some Modelling Issues

Four-node quadrilateral membrane elements (M3D4) were used to model the surface of the balloon. For each truncated isotensoid, 25 nodes were arranged along the meridian —their coordinates being defined by Equations 1 and 2— and were rotated about the z-axis to generate a mesh of 24×32 elements for each isotensoid. ABAQUS also provides reduced integration membrane elements (M3D4R), which may be more efficient than M3D4 in terms of computational time. However, the performance of this element in combination with Adler's IMP subroutine is not known.

Beam elements (B31) were used to model the top and bottom plates, i.e. to connect to a central point the nodes along the top/bottom edges of the stack. Adjacent circumferential nodes were similarly connected by beam elements. Thus, the whole balloon structure is modelled such that it has stiff top and bottom "caps". The use of shell elements (S4R, S3) to form these caps was investigated, but poor convergence was observed.

Truss elements (T3D2) were used to form a stiffening hoop along the seam between consecutive truncated isotensoids. Also, a stiff pin-jointed truss element was used to hold the top cap at a fixed distance from the bottom one, while allowing it to move sideways and to rotate.

Details on the element properties are given in Table 1.

	Membrane	Beam	Truss
Thickness t (mm)	0.05		
Cross-sectional dimensions (mm)		100×100	100×100
Young's modulus, E (N/mm^2)	3,500	215,000	215,000
Shear modulus, G (N/mm^2)	1350	80,000	80,000
Poisson's ratio, ν	0.3	0.35	0.35

Table 1
Material properties

The first step of the analysis consisted in inflating the balloon to a certain pressure, at which the truncated isotensoids take up an initial shape such that the stress distribution is purely meridional. Two ways to achieve this in ABAQUS were investigated, as follows.

The first method prescribes the correct initial stress in each element by means of the *INITIAL CONDITION option. The corresponding initial pressure is applied by follower forces using *DLOAD. A non-linear incremental analysis is then carried out, which ends when the balloon has reached the required stress level under the prescribed pressure.

The second method sets up the balloon initially unstressed, and simulates its pressurization with the modified version of the IMP subroutine, explained in the previous section.

Both methods have been found to work well, but the former suffers from the limitation that, once a material subroutine is used, ABAQUS requires that a user-defined material subroutine be used throughout the analysis. Hence, because the standard IMP subroutine is needed for a subsequent part of the simulation, the latter method had to be adopted.

To avoid that the boundary conditions affect the stress distribution in the structure during pressurization, only one end of the central pin-jointed bar was fixed. After pressurization, the response of the balloon to different geometric imperfections was analysed and, to avoid that different parts of the balloon go through one another, it is essential to properly model the contact conditions. The three top and bottom rings of elements in each isotensoid were defined as contact surfaces, using the *SURFACE option; the *SURFACE INTERACTION option was used to define the type of interaction; and finally the *CONTACT PAIR option was used to indicate which pairs of surfaces can come into contact.

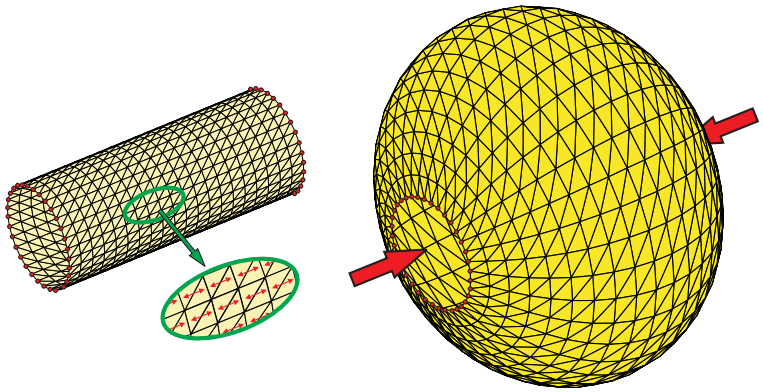

Fig. 8. Inflation of cylinder with wrinkle lines in longitudinal direction.

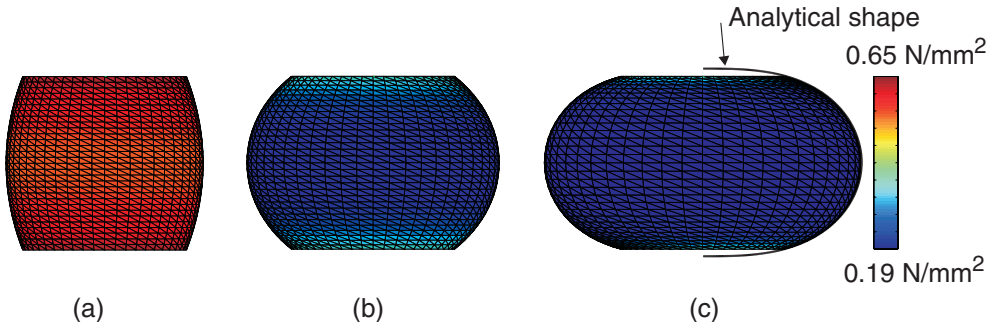

Fig. 9. Truncated isotensoids generated with inflation pressures of 0.75, 10, and 37.5 Pa, with contours of σ_ϕ due to $p = 5$ Pa.

5 Stability in Initial Configuration

The wrinkled membrane element presented in Section 3 can be used to generate a truncated isotensoid by setting up a cylindrical membrane, defining the wrinkle directions to be parallel to the axis of the cylinder, and applying an internal pressure, see Figure 8.

Depending on the magnitude of the pressure applied and the elastic stiffness of the membrane, different shapes are obtained. The three surfaces shown in Figure 9 were all obtained starting from a 4.2 m long cylinder with a radius of 2.0 m. The figure shows that the surface in Figure 9(c) is a piece of an isotensoid surface.

Consider the surface shown in Figure 9(c), whose meridian has an arc-length of 5 m. A comparison between the analytical distribution of σ_ϕ, from Equation 4, with the meridional stresses obtained from a Matlab (Mathworks 2002) finite-element program that implements this wrinkled element, shows the two distributions to be essentially identical.

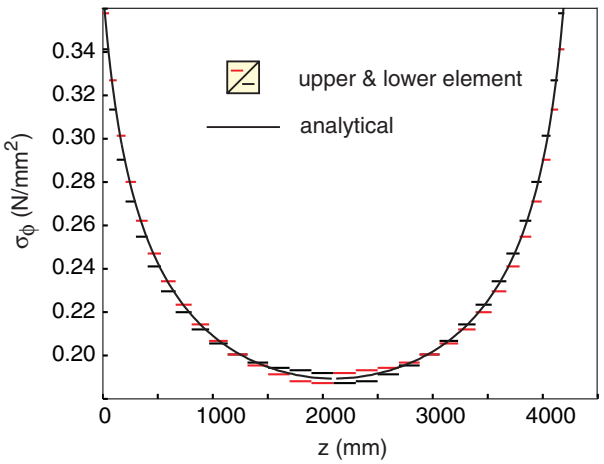

Fig. 10. Comparison between analytical and numerical distribution of σ_ϕ ($p = 5$ Pa).

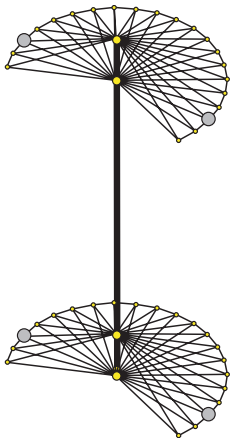

Fig. 11. Arrangement of pin-jointed bars at top and bottom of truncated isotensoid or isotensoid stack, showing 4 kinematic constraints.

5.1 Truncated Isotensoid

The stability of an elastic structure in a given configuration and state of stress is related to the positive definiteness of its stiffness operator, and hence to the eigenvalues of its tangent stiffness matrix being positive (Riks 1998).

We have carried out such an analysis for the truncated isotensoid of Figure 9(c). The nodes along the top and bottom edges were connected to a kinematically determinate arrangement of pin-jointed bars, connected to a central pin-jointed bar, see Figure 11.

First, we determined the eigenvalues and corresponding eigenvectors of the (non-symmetric) tangent stiffness matrix of this structure using the function `eigs` (Mathworks 2002). The tangent stiffness matrix of the membrane was based on the wrinkled membrane element presented in Section 3. The eigenvectors corresponding to the smallest eigenvalues, which correspond to the

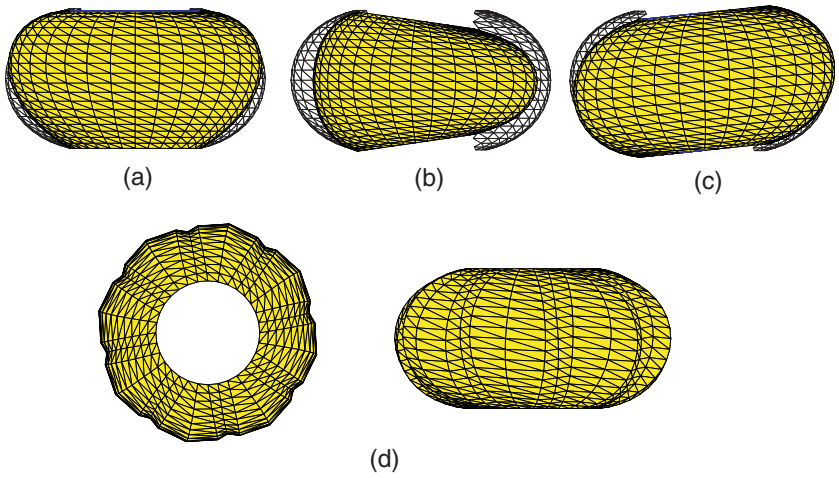

Fig. 12. Side views of eigenvectors of truncated isotensoid (wrinkled material model); undeformed shape shown dotted. For the local mode in (d) a top view is also shown.

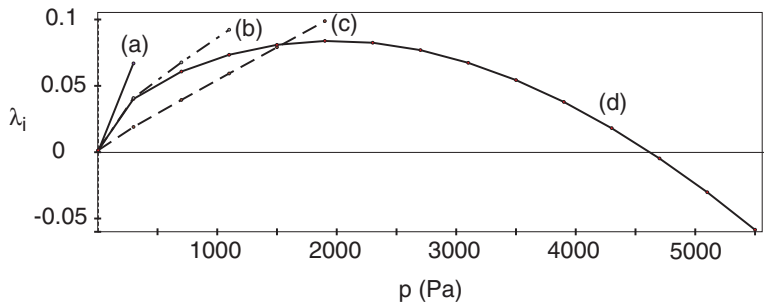

Fig. 13. Variation of eigenvalues with pressure in a truncated isotensoid (wrinkled material model). Other local modes are similar to (d).

incipient "buckling modes" of the structure. These eigenvectors can be divided into two categories, namely global modes —shown in Figure 12(a-c)— and local, or wrinkling modes — of which a sample is shown in Figure 12(d).

The global eigenvectors, of which only a small number have very small eigenvalues, involve overall distortion of the surface, such as twisting or lateral swaying of the upper edge with respect to the bottom edge. The local eigenvectors involve coupled hoop-wise and radial distortion of the meridians of the isotensoid, in an n-fold symmetric mode. There is a large number of this type of eigenvectors, which further increases if the mesh density is increased.

Figure 13 shows the variation of the smallest eigenvalues with the pressure p. An interesting feature is that the structure is stable, i.e. all eigenvalues are positive, up to $p \approx 4600$ Pa. Note that all global modes become more stable when p increases, whereas the local modes become less stable.

Next, let us consider the same structure, but change the model to a standard isotropic material (thus implicitly assuming that the skin of the pressurized balloon is able to carry both tensile and compressive stress increments) then all

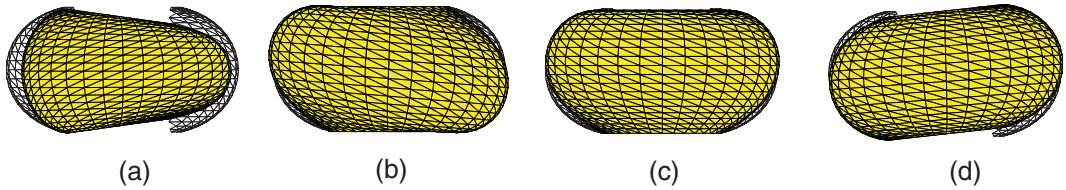

Fig. 14. Side views of eigenvectors of truncated isotensoid (isotropic material model); undeformed shape shown dotted.

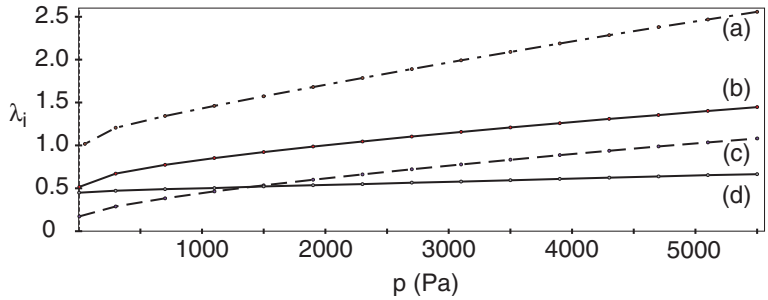

Fig. 15. Variation of eigenvalues with pressure in a truncated isotensoid (isotropic material model).

the eigenvalues increase substantially, mainly as a result of having considered a shear-stiff material, and the local modes disappear, Figure 14. Hence, since, the modes are all global, when the pressure is increased all modes become more stable, see Figure 15.

5.2 Stack of Truncated Isotensoids

The study in the previous section was extended to a stack of four isotensoids, each identical both in terms of geometry and material properties to the single isotensoid studied in Section 5.1. The boundary conditions at the top and bottom of the stack were the same as the top and bottom of the single isotensoid, but note that now the intermediate isotensoids are allowed to distort into a non-circular shape at either end.

If the wrinkled material model is used for the isotensoid stack, then again the eigenvectors corresponding to the smallest eigenvalues can be grouped into global —Figure 16(a-c)— and local —Figure 16(d-f)— deformation modes. Each type has similar characteristics to those noted for a single isotensoid.

Figure 17, showing the variation of the smallest eigenvalues with pressure, indicates that the global modes are intially less stable than the local ones, as the corresponding eigenvalues are now significantly smaller (even allowing for the decrease due to the four-fold increase in the number of degrees of freedom). Note that the eigenvalues of the local modes are substantially unchanged.

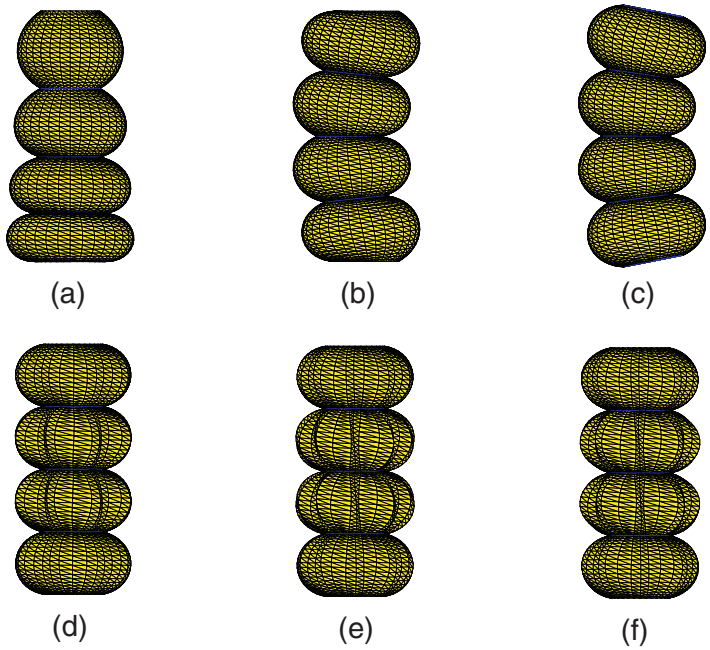

Fig. 16. Side views and top views of eigenvectors of stack of four truncated isotensoids (wrinkled material model).

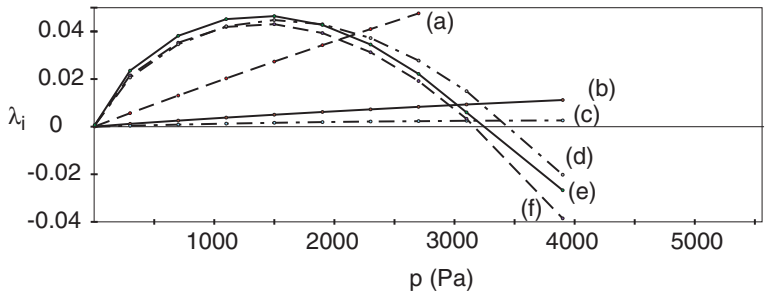

Fig. 17. Variation of eigenvalues with pressure in stack of four isotensoids (wrinkled material model).

However, as p increases, the global modes become gradually more stable while the local modes become less stable and finally unstable at $p \approx 3000$ Pa. Hence, it can be concluded that the four isotensoid stack is less stable than the single isotensoid.

The eigenvectors obtained from an isotropic material model of the isotensoid stack are shown in Figure 18. Again, there are only global modes and all eigenvalues are positive and increasing with p.

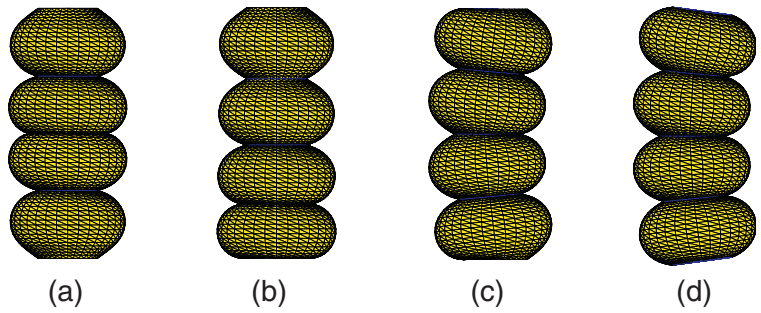

Fig. 18. Side views and top views of eigenvectors of stack of four truncated isotensoids (isotropic material model).

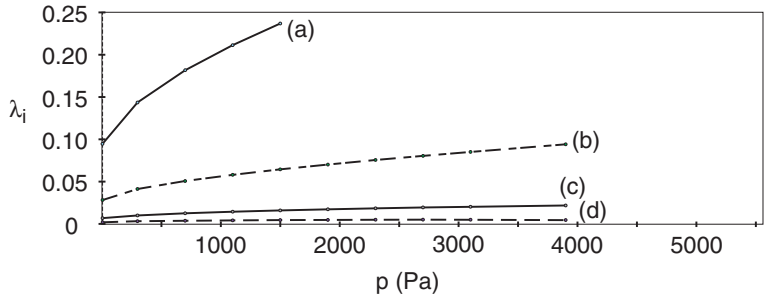

Fig. 19. Variation of eigenvalues with pressure in stack of four isotensoids (isotropic material model).

6 Non-Linear Simulations

This section presents the results of a series of simulations, with ABAQUS, of the response of an isotensoid stack to different geometric perturbations. These simulations are generally carried out as three separate steps:

- Pressurization to $p = 5$ Pa, accompanied by a small amount of elastic stretching of the material. Afterwards p remains constant.
- Distortion of the shape of the structure, by means of temporary geometric constraints, to trigger any unstable modes.
- Removal of any temporary constraints, to test the stability of the structure in the distorted configuration.

Note that no calculation of eigenvalues and eigenvectors is carried out, as the results would not be accurate because pressure is a follower-type load that leads to an unsymmetric load stiffness matrix. Eigenvalue extraction in ABAQUS can be performed only on symmetric matrices.

All of the analysis steps are geometrically non-linear, incremental simulations, using the *NLGEOM option. Automatic stabilization of any unstable modes through the addition of numerical damping is allowed, using the STABILIZE function. The amount of numerical damping was kept at the minimum required

to achieve convergence.

For the pressurization step, Figure 20 shows a comparison of the results obtained from the two different methods explained in Section 4.1. Both methods are successful in achieving a distribution of σ_ϕ that agrees with Equation 4. However, note that the initial stress method results in a small compressive σ_θ, whereas with the modified IMP subroutine $\sigma_\theta \approx 0$ everywhere.

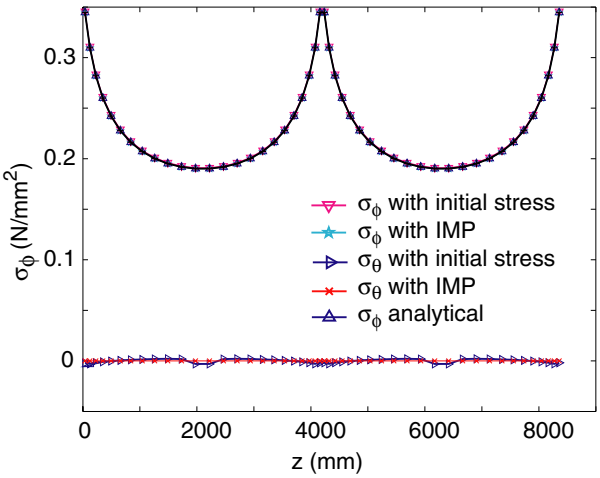

Fig. 20. Stress distribution in stack of two truncated isotensoids, after pressurization ($p = 5$ Pa).

In the second step, two different types of geometric distortions were investigated. The first type is a simple end-displacement, δ, of the top, central node of the balloon, see Figure 21(a). Note that all nodes along the bottom edge are constrained in this analysis. The second type of distortion is based on the buckling mode shape proposed by Lennon and Pellegrino (2000), see Figure 21(b). This distortion mode is based on the idea of imposing a uniform curvature to the central axis of the balloon, while keeping the circumferential hoops between adjacent isotensoids circular and perpendicular to the curved axis. The distance between the end points of the central pin-jointed bar is unchanged. Different amounts of distortion can be imparted by varying the angle between the two ends of the balloon, 2ψ. This shape is imposed by means of the *BOUNDARY option, by imposing suitable displacements to all the nodes lying on the hoops.

Note that the second step induces severe wrinkling in the balloon, and the use of a non-linear material model such as the standard IMP subroutine described in Section 4 is essential to avoid the presence of any compressive stresses.

Finally, in the third step all the temporary constraints imposed during the second step are removed using the *BOUNDARY, OP=NEW option, and a "restart" analysis is carried out to find out if the distorted shape is stable or not, in which case the balloon will seek an alternative equilibrium configura-

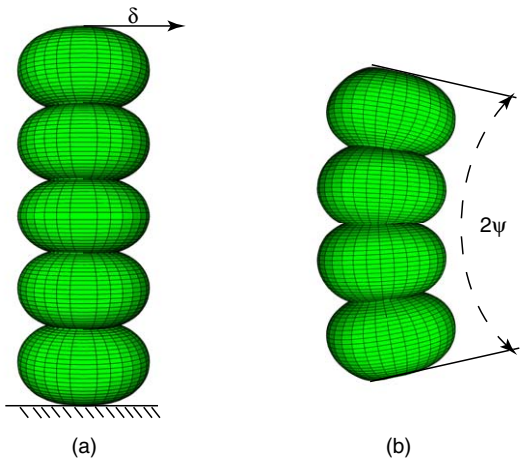

Fig. 21. Geometric perturbations.

tion. Only the original constraints are kept.

This analysis requires great care, to go past numerical instabilities while avoiding excessive numerical damping, which would change the outcome of the analysis. One of the tricks used to minimise this effect was to carry out further restart analyses, each with a lower STABILIZE factor.

6.1 Results

For the type of perturbation shown in Figure 21(a) many different analyses were carried out, varying the number of isotensoids in the stack, the magnitude of the imposed displacement, etc.

A set of typical results are shown in Figure 22, for a balloon consisting of five truncated isotensoids. This is a plot of the force that has to be applied at the top of the balloon versus the horizontal displacement at the same point, δ. It is interesting to note that when the displacement reaches about 0.1 m the stiffness of the balloon begins to decrease, but a positive stiffness is maintained despite a further increase of the displacement to 0.7 m. Further displacements were imposed, but are not shown here.

After releasing the temporary constraint, the results of two restart analyses are shown in the figure. When the higher (default) value of the STABILIZE factor was used the balloon maintained its distorted configuration, however when the lower factor was used, the balloon returned to its original configuration.

This analysis has shown that the particular stack of five isotensoids that has been analysed is rather weakly stable for the perturbation of Figure 21(a). It does not go back to its original configuration unless the numerical damping in the simulation is very small.

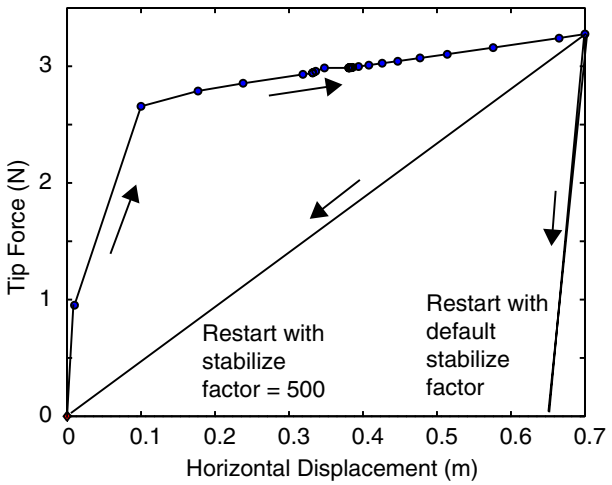

Fig. 22. Response of five-isotensoid balloon to imposed tip displacement, δ.

ABAQUS can display the contact area at each increment, and it is found that the isotensoids at the bottom of the stack come into contact when $\delta = 1.551$ m. However, a separate analysis which did not include modelling of contact was found to give an almost identical force-displacement relationship.

Next, we show the results obtained when the alternative perturbation, shown in Figure 21(b), was imposed. This analysis was repeated for two different values of the bend angle, $\psi = 7.5°$ and $\psi = 15°$, and in both cases the balloon did not return to the original configuration.

Figure 23 is a plot of the displacement of a node on the central hoop. During the first step, corresponding to the range 0 to 1 on the abscissa, the movement of the node is driven by the imposed constraints. During the second step, corresponding to the range 1 to 2 on the abscissa, the constraints are released and the node, instead of returning to its original position, gradually increases its displacement to about 2.4 m. Further restart analyses, with lower numerical damping were carried out, but the balloon maintained the shape of the last analysis step, which indicates that the structure is stable in its new configuration.

Figure 24 shows contour plots of the horizontal displacement components, drawn on top of the actual shape of the balloon, first when a perturbation amplitude $\psi = 7.5°$ is imposed, and then after completing the restart analysis. The final configuration is visibly more distorted than the initial one.

It was noted during the analysis that contact modelling is essential to achieve convergence during the final part of the third analysis step, as a model that did not include contact was unable to converge when all the constraints were released.

Following the analysis by Lennon and Pellegrino (2000), we have calculated

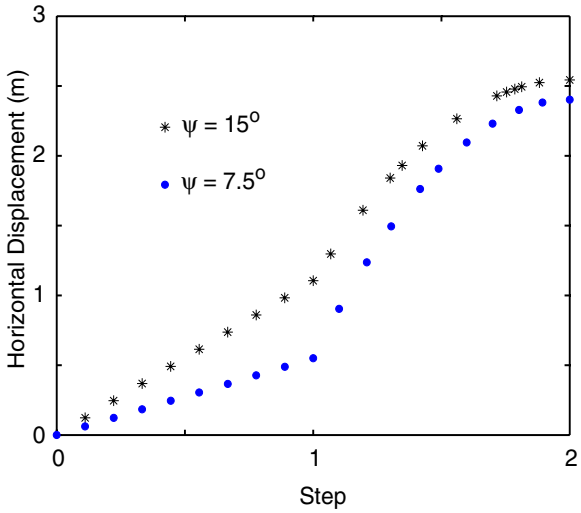

Fig. 23. Displacement of node on mid hoop.

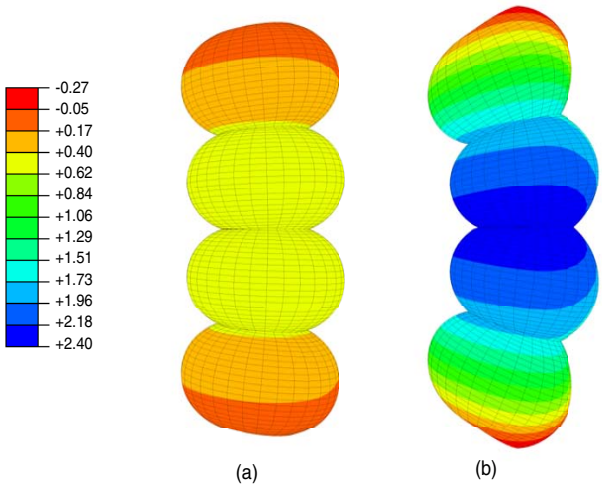

Fig. 24. Contours of horizontal displacements, in metres, for (a) initial perturbation mode and (b) final equilibrium shape.

the volumes of the four isotensoid stack in the three configurations that have been considered. The results of this calculation are listed in Table 2. It is shown that the buckled modes lead to smaller volumes. When all the constraints are released after introducing the imperfection modes, the total volume decreases even further.

Bend angle	$\psi = 7.5°$	$\psi = 15°$
Original volume after pressurization	591.96	591.96
Volume of distorted configuration	589.19	581.61
Final volume	575.57	571.151

Table 2
Volume of balloon (m^3)

7 Discussion and Conclusion

This paper has introduced two computational approaches to the stability analysis of lobed balloons, one based on a wrinkled material model —which has zero stiffness in the direction perpendicular to the wrinkles and also in shear— and one based on a variable Poisson's ratio model that eliminates compressive stresses iteratively. The first approach has been implemented in Matlab, the second approach has been implemented through a user-defined material model in the ABAQUS finite-element package. Both approaches have been shown to be able to produce the analytically known initial stress distribution of the isotensoid.

The first approach has been used to investigate the stability of both a single isotensoid and a stack of four isotensoids, for perturbations of infinitesimally small amplitude. It has been found that both structures are stable for global deformation modes, but unstable for local modes at sufficiently large pressure. The local deformation modes disappear if —instead of using a wrinkled material model— an isotropic model is assumed. For this latter model, both structures have been found to be stable.

An important observation is that the wrinkled material model predicts much smaller eigenvalues —due to the lack of shear stiffness— and hence a much less stable structure.

The second approach has been used to investigate the stability of the two structures for large shape perturbations, and here a key point is that contact between different surfaces of the balloon has been properly accounted for. It has been found that, even when analysing a structure that is known to be stable in some distorted configurations, it is not a straightforward matter to pick out the deformation path that will take the structure away from its initial configuration. Part of the problem is that these alternative, stable, distorted configurations have been found to enclose a smaller volume and hence will probably correspond to a local energy minimum for the structure. Such local minima can only occur as a result of the unilateral constraints associated with surface contact, which usually are activated only by large shape distortions.

Although this last result may seem surprising at first, as it is usually argued that balloon structures subject to uniform pressure will achieve the shape that maximises the enclosed volume, it is actually supported by analyses of the telemetry data from pumpkin balloons that had deployed into a clefted configuration.

Acknowledgements

This research was partially supported by the NASA Balloon Program Office (BPO) and the NASA National Scientific Balloon Facility, Program Monitor Mr Danny Ball.

We thank Mike Smith (Raven Industries), Steve Smith (formerly at NASA BPO) and David Wakefield (Tensys) for many useful discussions.

References

ABAQUS (2003). ABAQUS Version 6.3. ABAQUS, INC. 1080 Main Street Pawtucket, Rhode Island 02860-4847 USA, Pawtucket, RI 02860

Adler, A.L. (2000). Finite element approaches for static and dynamic analysis of partially wrinkled membrane structures, PhD Dissertation, University of Colorado at Boulder.

Calladine, C.R. (1988). Stability of the Endeavour balloon. In: *Buckling of structures*, I. Elishakoff et al., eds., Elsevier Science Publishers, 133-149.

Lennon, B.A., and Pellegrino, S. (2000) Stability of lobed inflatable structures. 41st AIAA/ASME/ASCE/AHS/ASC Structures, Structural Dynamics and Materials Conference, 3-6 April 2000, Atlanta GA, AIAA 2000-1728.

MathWorks (2002). *Matlab User's Guide, version 6*. South Natick, MA.

Miller, R.K., and Hedgepeth, J.M. (1982). An Algorithm for Finite Element Analysis of Partly Wrinkled Membranes. *AIAA Journal*, **20** (12), 1761-1763.

Miller, R.K., Hedgepeth, J.M., Weingarten, V.I., Das, P., and Kahyai, S. (1985). Finite element analysis of partly wrinkled membranes. *Computers & Structures*, **20** (1-3), 631-639.

Nott, J. (2004). Design considerations and practical results with long duration systems for manned world flights. *Advances in Space Research*, **33**, 1667-1673.

Riks, E. (1998). Buckling analysis of elastic structures: a computational approach. In: *Advances in Applied Mechanics*, 1-72. Academic Press, Delft, The Netherlands.

Schur, W.W. (2004). Experimental investigation of undesired stable equilibria in pumpkin shape super-pressure balloon designs. *Advances in Space Research*, **33**, 1682-1687.

Stein, M., and Hedgepeth, J.M. (1961). Analysis of partly wrinkled membranes. NASA Langley Research Center, NASA TN D-813.

Taylor, G.I. (1919). On the shapes of parachutes. Reprinted in: *The Scientific Papers of Sir G.I. Taylor*, Vol. 3 (1963), G.K. Batchelor , ed., 26-37, Cambridge University Press.